



# Simple shear origin of the cross-faults ruptured in the 2019 Ridgecrest earthquake sequence

Yuri Fialko D M and Zeyu Jin D

Observations in tectonically active areas increasingly reveal sets of high-angle conjugate faults ('cross-faults') that apparently contradict theories of faulting based on experimental data. Possible explanations include a low in situ coefficient of friction, dominant control of ductile shear zones in the lower crust, and tectonic rotation. Discrimination between these mechanisms has been hindered by uncertainties in the state of stress, deformation history and fault geometry at seismogenic depths. Here we use a combination of seismic, geodetic and geologic data to demonstrate that ubiquitous cross-faults in the Ridgecrest (California) area, including those ruptured in the sequence of strong earthquakes in 2019, result from rotation from an initially optimal orientation consistent with experimental data. The inferred rotation pattern can be explained by the geodetically measured velocity field. Our model suggests that the observed asymmetric rotation of faults in the Eastern California Shear Zone can result from simple shear. The same mechanism can be responsible for high-angle conjugate faults observed in other tectonic settings.

arthquakes result from unstable slip on faults that are brought to failure by the ambient stress field; however, relationships between causal stresses and the consequent seismic ruptures are not well understood. Mohr-Coulomb-Anderson theory predicts that faults should form at an acute angle with respect to the principal compression axis<sup>1,2</sup>. Such an 'optimal' angle  $\theta_0$  depends solely on the coefficient of friction  $\mu$ , where  $\theta_0 = \pm 0.5 \arctan(\mu^{-1})$ . For typical laboratory values of the coefficient of friction of 0.6–0.8 (Byerlee's law)<sup>3</sup>, the respective angle is  $|\theta_0| \approx 25-30^\circ$  (refs. <sup>2,4</sup>). New faults that are produced in laboratory experiments at a scale of 10<sup>-2</sup>-10<sup>-1</sup> m and in nature at a scale of 1-10<sup>3</sup> m appear to agree with predictions of Mohr-Coulomb-Anderson theory<sup>5-7</sup>. However, mature (well-slipped) faults are often severely mis-oriented with respect to the present-day stress field8-11, implying the rotation of faults with respect to the principal stress axes, rotation of the principal stress axes, or both, throughout the fault history<sup>12</sup>. Mature faults can operate at high angles with respect to the principal compression axis (and therefore at low resolved shear stress) if they are substantially weaker than the host rocks, owing to either static 13-15 or dynamic 16-19 weakening mechanisms. Many of the proposed weakening mechanisms require extreme localization of slip within a fault zone<sup>20</sup> and such localization may in turn depend on fault maturity<sup>21</sup>. If so, an outstanding question is, at which point during a fault evolution may various weakening mechanisms become activated? Alternatively, faults might be weak from their inception<sup>22</sup>, implying that either the coefficient of friction is well below the experimentally measured values of 0.6-0.8 (refs. 3,23) or the pore fluid pressures are well above the hydrostatic pressure. These possibilities can in principle be distinguished by evaluating the orientation of incipient faults with respect to the principal stress axes. As the latter may not be well known, one can instead use the relative orientation of conjugate faults, under the assumption that the principle compression axis bisects the angle between conjugate planes<sup>2,24</sup>. Unfortunately this approach is not easily applicable to fossil conjugate fault zones because it is not always clear whether or not different sets of faults were active at the same time. The relationships between active conjugate faults could be studied using seismic focal

mechanisms; however, uncertainties in the fault plane solutions are typically too large, especially for small- to intermediate-size events. Also, the focal mechanisms are essentially indistinguishable in the case of high-angle conjugate faults<sup>25</sup>. An optimal data set for a case study would thus involve a sequence of earthquakes that occur on conjugate faults that are relatively immature, yet the earthquakes are large enough not to be treated as point sources. These (rather restrictive) criteria were met during the 2019 Ridgecrest, California, earthquake sequence, which has offered an excellent opportunity to investigate the problem of in situ fault strength.

# Conjugate faulting in the Ridgecrest area

The 2019 Ridgecrest, California, earthquake sequence occurred on a network of northwest-trending right-lateral and northeast-trending left-lateral strike-slip faults<sup>26–28</sup>. The largest events in the sequence were the  $M_{\rm w}$  6.4 foreshock and the  $M_{\rm w}$  7.1 mainshock (Fig. 1a). The seismic moment release due to the  $M_{\rm w}$  7.1 mainshock was dominated by slip on right-lateral faults, and the seismic moment release due to the  $M_{\rm w}$  6.4 foreshock was dominated by slip on left-lateral faults<sup>28</sup>. Both the foreshock and the mainshock involved slip on antithetic cross-faults<sup>26,29</sup>. Events comprising the 2019 sequence occurred on immature and largely unmapped faults that were not previously recognized as connected and capable of major earthquakes<sup>30</sup>. The angle between the left- and right-lateral faults ruptured by the  $M_{\rm w}$  6.4 foreshock and the  $M_w$ 7.1 mainshock is close to 90°, so that the focal mechanisms based on the moment tensor solutions (see the 'Data availability' section) are essentially similar (Fig. 1a). However, because of the earthquake size the sense of motion is unambiguous from the aftershock distribution, as well as surface displacements imaged by field studies and space geodetic observations (Fig. 1b).

We quantified the dihedral angle between faults that produced the foreshock and the mainshock using seismic, geodetic and geologic data, as well as finite fault models informed by all of the available data (see the 'Evaluating the attitude of the 2019 ruptures' section in the Supplementary Information). The admissible range of angles is 75–100°, with the preferred value of about 85° (Supplementary Fig. 2). As the 2019 Ridgecrest earthquake sequence occurred

Institute of Geophysics and Planetary Physics, Scripps Institution of Oceanography, University of California San Diego, La Jolla, CA, USA. e-mail: yfialko@ucsd.edu

ARTICLES NATURE GEOSCIENCE

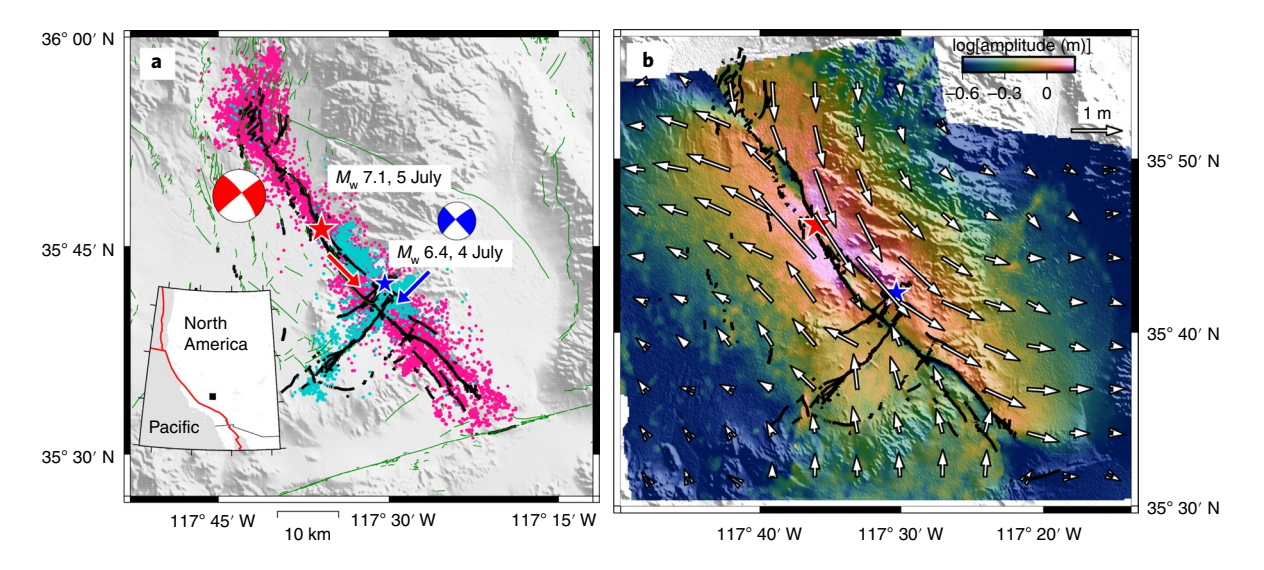


**Fig. 1** Aftershocks and coseismic surface displacements due to the 2019 Ridgecrest earthquakes. a, Map of the epicentral area. Black wavy lines denote surface offsets due to the Ridgecrest earthquakes mapped by field surveys<sup>30</sup>. Red and blue stars denote the epicentres of the  $M_w$  7.1 and  $M_w$  6.4 earthquakes, and red and blue 'beach balls' and arrows denote the focal mechanisms and the average fault strikes, respectively. Teal and magenta dots denote the aftershocks of the  $M_w$  6.4 and  $M_w$  7.1 events, respectively<sup>26</sup>. Thin green lines denote mapped active faults<sup>44</sup>. The inset shows the site location (black square) with respect to the plate boundary (red line). **b**, Coseismic displacements derived from space geodetic data (see Methods). Colour denotes the logarithm (base 10) of the amplitude of horizontal displacement<sup>45</sup>, in metres ( $10^{-0.6} \approx 0.25 \, \text{m}$ ,  $10^{-0.3} \approx 0.5 \, \text{m}$ ), and arrows denote the displacement vectors on a sub-sampled grid. Vertical displacements are shown in Supplementary Fig. 1.

within a densely instrumented area featuring long-lived seismic and geodetic networks (Supplementary Fig. 3), additional insights can be gained regarding the fault orientation with respect to the principal stress axes. Inversions of focal mechanisms of abundant small local earthquakes indicate an approximately north-south orientation of the maximum horizontal compressive stress  $\sigma_{\rm Hmax}$  (ref. <sup>31</sup>). We used 15-year-long time series of displacements from the Plate Boundary Observatory (PBO) network to compute the principal axes of strain rate (see the Methods section and Supplementary Figs. 4 and 6). The axis of the maximum horizontal shortening rate  $\dot{\epsilon}_{\rm Hmax}$  in the neighbourhood of the 2019 rupture is oriented ~5° east of north (Supplementary Fig. 6). The estimated trajectories of  $\sigma_{\rm Hmax}$ and  $\dot{\epsilon}_{\rm Hmax}$  are shown in Fig. 2, along with the precisely relocated background seismicity<sup>31</sup>. The principal compression and shortening axes are in general agreement, except in areas with sparse seismicity and/or PBO station coverage (for example, in the southwest corner of Fig. 2). Around the epicentre of the  $M_{\rm w}$  7.1 mainshock, the orientations of  $\sigma_{\rm Hmax}$  and  $\dot{\epsilon}_{\rm Hmax}$  are essentially north-south, with the contraction rate axis possibly oriented slightly more easterly compared with the compression axis. Within the uncertainties, the  $\sigma_{H_{max}}$  and  $\dot{\epsilon}_{\rm Hmax}$  axes bisect an angle formed by the cross-faults ruptured by the 2019 Ridgecrest earthquakes (Supplementary Fig. 2).

# Mechanisms responsible for the development of cross-faults

Previous studies have suggested that the pattern of high-angle faulting observed during the 2019 sequence results from either a near-zero coefficient of friction, so that the crustal strength is limited to cohesion, or rock failure due to dynamic stress perturbations near a propagating rupture front<sup>26</sup>. While the latter might be responsible for small-scale 'wing' faults oriented at high angle with respect to the main rupture<sup>32</sup>, it does not apply to the two largest events of the 2019 sequence that were separated by a day (Fig. 1a). Also, inspection of previous background seismicity reveals a number of lineated structures that closely follow the strike of the right- and left-lateral faults ruptured during the 2019 sequence (Y.F., manuscript in preparation). Several of such lineations are marked by the red and blue dashed lines in Fig. 2. These observations indicate a

widespread distribution of active cross-faults in the Ridgecrest area that cannot be attributed to the effects of dynamic off-fault yielding.

Another possible explanation for the nearly orthogonal fault orientation is strain localization in the ductile lower crust<sup>33,34</sup>. If the strength of the continental crust is dominated by a ductile substrate, the development of ductile shear zones may dictate fault orientations in the upper brittle crust. Since the ductile rheology is essentially independent of the mean stress, shear zones are expected to align at 45° with respect to the principal stress axes, thus forming a right angle between the conjugate shear zones. Several lines of argument, however, suggest that this mechanism is unlikely to be responsible for the observed fault geometries in the Ridgecrest area. First, a potential for strain localization in the ductile regime is inversely proportional to the effective viscosity<sup>35</sup>. Localized shear zones are less likely to form in a warm stretched crust such as that in the Ridgecrest area, characterized by recent volcanism and ongoing geothermal activity<sup>36</sup>. Second, ductile shear zones are unlikely to develop below immature low-slip-rate faults, especially small, broadly distributed, low-offset faults such as those abundantly present in the Ridgecrest area (Fig. 2). Finally, even if multiple conjugate faults were associated with deep ductile roots, the respective network of intersecting ductile shear zones would not be able to preserve its geometry under finite strain.

It might be tempting to interpret ubiquitous high-angle faults in the Ridgecrest area, including the 2019 ruptures (Fig. 2), as well as their orientation with respect to the principal compressive stress (Supplementary Fig. 2) in terms of a low coefficient of friction in the upper crust. If the observed active faults represent failure on optimally oriented planes (that is,  $2\theta_{\rm o} > 75^{\rm o}$ ), the respective coefficient of friction  $\mu$  is smaller than 0.3, well below the experimentally determined values for most rock types<sup>3,23</sup>. If so, this would have profound implications for the mechanics of faulting and the strength of the brittle part of the lithosphere. Below we demonstrate that the angle between cross-faults involved in the Ridgecrest sequence is not an optimal angle for Mohr–Coulomb failure, and that the brittle strength of the seismogenic crust is in agreement with Byerlee's law at the onset of faulting.

NATURE GEOSCIENCE ARTICLES

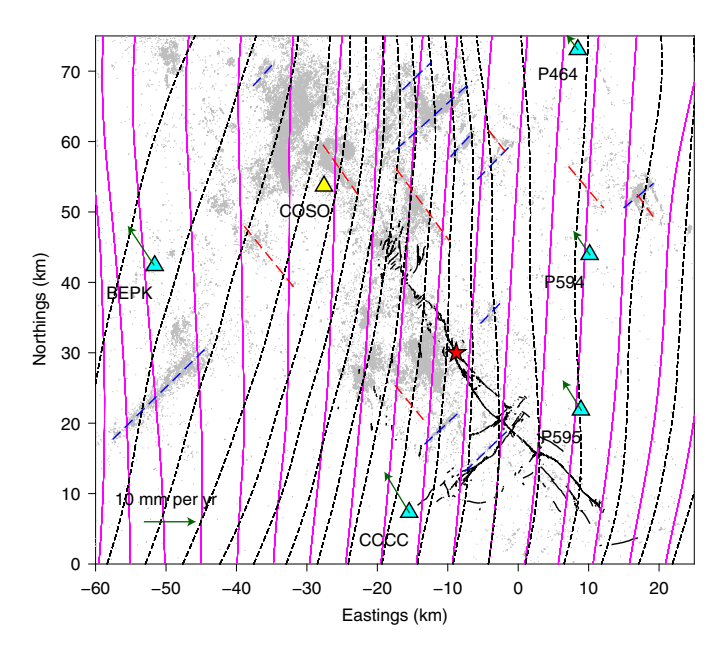


**Fig. 2** | Orientation of the principal stress and strain rate axes in the 2019 mainshock area. Black dashed lines denote trajectories of the maximum horizontal compression ( $\sigma_{Hmax}$ )<sup>31</sup>, magenta lines denote the direction of the maximum horizontal shortening rate ( $\dot{e}_{Hmax}$ , see Methods) and grey dots denote the background seismicity (from 1981 to June 2019)<sup>46</sup>. Filled triangles and green arrows denote the location of continuous Global Navigation Satellite System sites and secular velocities (with respect to site SHOS; see Supplementary Fig. 3). Black solid lines denote surface traces of the 2019 Ridgecrest earthquakes. Blue and red dashed lines denote lineations in the background seismicity that are parallel to the left- and right-lateral faults involved in the 2019  $M_w$  6.4 foreshock and the  $M_w$  7.1 mainshock, respectively (see Fig. 1). The local origin is at 117.5° W, 35.5° N.

# Fault rotation from long-term tectonic deformation

Theoretical considerations confirmed by observations suggest that tectonic deformation that promotes faulting, over time, gives rise to a rotation of active faults away from the shortening axis<sup>37,38</sup>. The amount of rotation depends on the rate of deformation and the fault age. We use the modern deformation rates calculated using the Global Navigation Satellite System (GNSS) data (Supplementary Figs. 3-6) to estimate the time required to rotate conjugate faults from an initially optimal orientation  $(2\theta_0 \approx 50-60^\circ)$ to the observed configuration  $(2\theta \approx 75-90^{\circ})$ ; Supplementary Fig. 2). As a preliminary step, we develop an analytic solution for the case of pure shear (see the 'Fault rotation under pure shear' section in the Supplementary Information). The results are shown in Supplementary Fig. 7. Given the present-day shortening rate of around 3×10<sup>-2</sup> Myr<sup>-1</sup> (Supplementary Fig. 5), optimally oriented faults are expected to rotate by 10-15° over a time period of the order of 5-10 Myr (Supplementary Fig. 7). The resulting rotation is symmetric with respect to the shortening axis. The estimated age of rotation agrees well with time elapsed since the inception of the Eastern California Shear Zone (ECSZ)39, suggesting that the currently active cross-faults (Figs. 1 and 2) may indeed have formed at optimal angles with respect to the compression axis in the early stages of the initiation of the ECSZ, and subsequently rotated toward their current (non-optimal) orientations.

To explore this possibility further, we performed calculations in which we relaxed a number of simplifying assumptions. In particular, instead of the infinitesimal strain rate tensor, we used secular velocities measured using the GNSS (Fig. 2 and Supplementary Fig. 4) to track the rotation of linear markers that were initially optimally oriented with respect to the principal compression axis.

The only assumptions behind this model are that (1) the present-day deformation is indicative of deformation over the past several million years and (2) the principal compression axis is the same as the principal shortening axis. Figure 3a shows the predicted fault orientations (thin coloured lines, solid and dashed) as a function of time, for the past 6 Myr. Also shown for reference are the surface traces (red and blue solid lines) of the best-fit fault model of the 2019 Ridgecrest events<sup>28</sup>. While the relative rotation between the left- and right-lateral conjugate faults predicted by the long-term tectonic deformation model is able to explain the observed angles between faults ruptured during the Ridgecrest sequence, as well as other active faults in the area (Fig. 2), the individual fault strikes predicted by the rotation model do not quite match the observed ones (Fig. 3a).

From Fig. 3a, one can notice that a better agreement can be rendered by a modest anticlockwise rotation of the entire set of thin coloured lines. This is equivalent to suggesting that the orientation of the principal compression axis at the time of inception of the ECSZ was slightly different from its current orientation, suggested by inversions of the earthquake focal mechanism data (Fig. 2). Figure 3b presents a model in which new faults are formed at optimal angles (assuming a typical value of the coefficient of friction  $\mu$  of 0.6) with respect to the  $\sigma_{Hmax}$  axis oriented 5° west of north. In this case, a good match between the predicted and observed fault geometries is obtained at 5 Myr after the fault initiation (purple lines in Fig. 3b). The inferred origin time is a function of the deformation history, but we note that values between 5 Myr ago (a constant strain rate) and 10 Myr ago (a linear increase from zero to the present-day strain rate) likely bracket a possible range of deformation histories, and are in excellent agreement with geologic constraints (6–10 Myr)<sup>39</sup>. The sensitivity of model predictions to the assumed values of the coefficient of friction is evaluated in Supplementary Fig. 8.

Our analysis shows that the initial model assumptions were not strictly valid. Both the  $\sigma_{Hmax}$  and  $\dot{\epsilon}_{Hmax}$  axes likely underwent a small clockwise rotation since the onset of faulting caused by reorganization of the plate boundary and the formation of the ECSZ. Recall that in the epicentral area of the 2019 Ridgecrest earthquakes, the shortening rate axis is oriented more easterly compared with the compression axis (Fig. 2 and Supplementary Fig. 2). While the difference in orientations is likely within the data uncertainties, we note that for a non-stationary deformation scenario the axes of compression and instantaneous shortening do not need to coincide.

## Geologic evidence of finite strain

The results shown in Fig. 3 suggest that the fault-rotation model is a reasonable explanation for the observed fault geometry. However, they alone do not rule out an alternative hypothesis, namely that the currently active cross-faults are optimally oriented for failure. The key discriminant between the two interpretations is the fault age. While it may be difficult to constrain the total offset for all of the linear features expressed in microseismicity (Fig. 2), there is geologic evidence indicating that cross-faults that broke the Earth's surface have accommodated finite strain commensurate with the total amount of shear since the inception of the ECSZ. Figure 4 shows a satellite photograph of an outcrop at the eastern end of the northeast-striking left-lateral fault system ruptured by the  $M_w$  6.4 foreshock. The outcrop features several igneous dikes that have the same trend as the Independence dike swarm, an extensive dike swarm in eastern California emplaced around 150 Myr ago<sup>40</sup>. The exposed dikes are offset by left-lateral faults that have the same trend as the northeast-striking cross-faults ruptured in 2019 (Fig. 4 and Supplementary Fig. 9), and some of the faults that cut the dikes were indeed activated by 2019 earthquakes (for example, Supplementary Fig. 9a). The apparent average spacing between the faults of approximately 50-200 m and the average offsets of the ARTICLES NATURE GEOSCIENCE

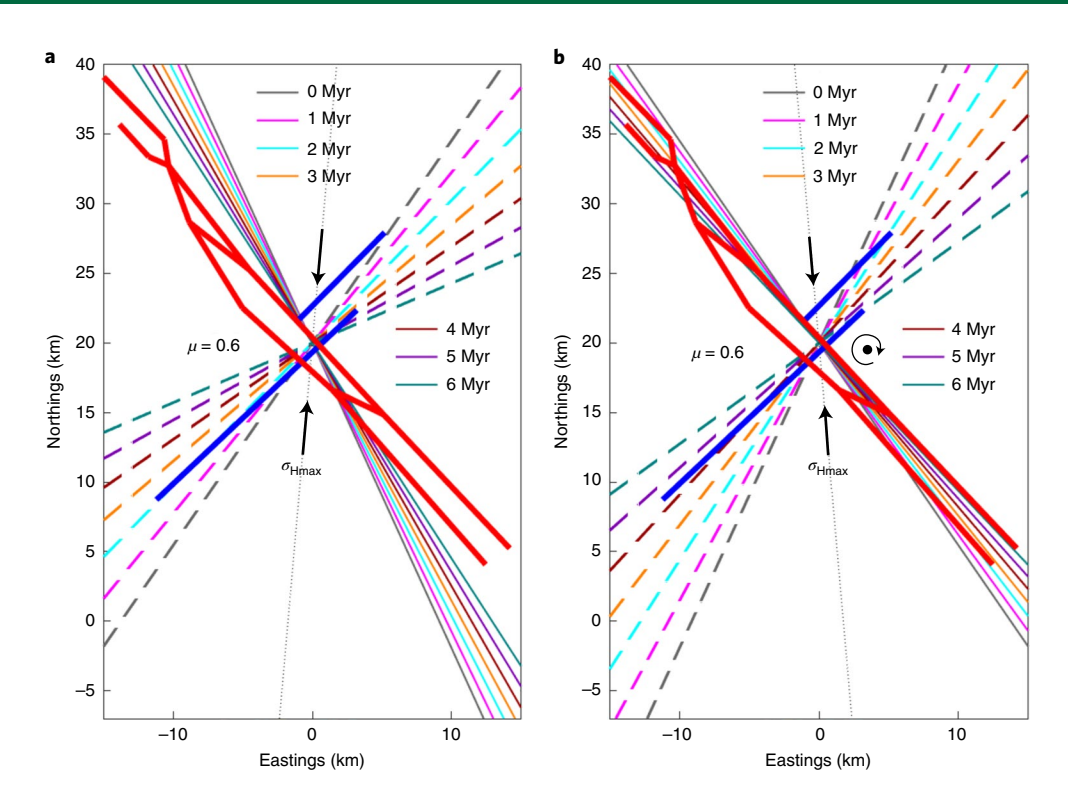


**Fig. 3 | Fault rotation predicted by extrapolation of the present-day velocity field into the geologic past. a**, Orientations of right- and left-lateral faults (thin solid and dashed lines, respectively) as a function of time since their formation at an optimal angle with respect to the principal compression axis (black dotted line; assumed to be coincident with the present-day shortening rate axis). Thick red and blue lines denote surface traces of the right- and left-lateral faults from the best-fit slip model of the 2019 Ridgecrest earthquakes<sup>28</sup>. **b**, Same as **a**, except that the maximum compression axis at the onset of faulting is oriented 5° west of north.

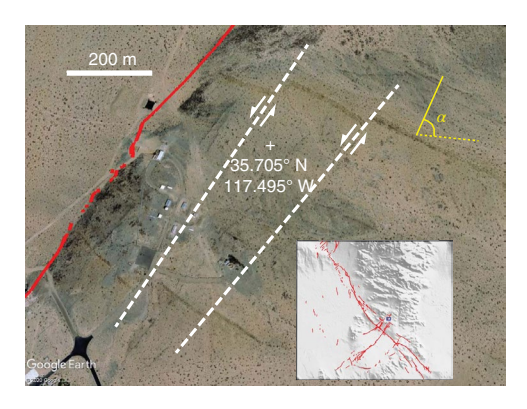


**Fig. 4 | Finite strain and rotation recorded by offset dikes.** Satellite photo of a dike swarm offset by left-lateral faults (white dashed lines) that have the same attitude as the 2019 left-lateral rupture that produced the  $M_{\rm w}$  6.4 foreshock (red line). The parameter  $\alpha$  is the angle between the axes of the least compressive stress acting at present (dashed yellow line) and at the time of the dike emplacement (solid yellow line). The white cross marks the indicated coordinates. The inset shows the outcrop location (blue rectangle) with respect to the entire earthquake rupture (red lines). The photograph is from Google Earth.

order of a few tens of metres (Fig. 4) indicate that the faults have accommodated shear strain of the order of 10%. This is comparable to the total shear strain produced by integrating the present-day deformation field (Fig. 2 and Supplementary Fig. 6) over the lifetime of the ECSZ (that is, several million years). Additional geologic and geomorphologic evidence also exists regarding the longevity of the right-lateral fault system<sup>30</sup>. These arguments lend further

support to the hypothesis that the abundant cross-faults identified in the Ridgecrest area formed in the early stages of the ECSZ at optimal angles with respect to the principal compression axis, remained active over the past several millions of years and were gradually rotated to their current configuration by the long-term tectonic motion.

A notable feature of fault rotation predicted by the models shown in Fig. 3 is a pronounced asymmetry between the right- and left-lateral fault systems. Right-lateral faults essentially preserve their orientation throughout geologic time, whereas left-lateral faults accommodate most of the rotation. This is a well-recognized but poorly understood feature of deformation in the ECSZ<sup>12</sup>. In the case of pure shear, the two sets of conjugate faults are expected to rotate symmetrically with respect to the shortening axis. Ron et al. 12 proposed that the observed asymmetry is caused by a large (20–25°) rotation of the principal stress axis coeval with faultling. Our model naturally explains the asymmetry due to the fact that deformation in the ECSZ is closer to simple shear rather than pure shear (Fig. 2). Because simple shear intrinsically involves rotation<sup>41</sup>, pure shear combines destructively with rotation due to axial shortening in the case of right-lateral faults and constructively in the case of left-lateral faults, producing the observed asymmetry (Fig. 3). This may also explain why right-lateral faults grow into connected structures that ultimately dominate the seismic moment release in the ECSZ, while left-lateral faults tend to be disrupted and disorganized as they rotate away from the favourable orientation. An eventual deactivation of left-lateral faults may be delayed by the onset of enhanced weakening (either static or dynamic). Conditions for the onset of enhanced weakening are poorly understood, but are likely related to the shear localization and structural maturity of fault zones, the evolution of porosity, mineral alteration, and so on. The persistence of slip on faults that formed at optimal angles and are now at around 45° to

NATURE GEOSCIENCE ARTICLES

the principal stress axis (Fig. 2) suggests some form of enhanced weakening, in particular because the rotated faults co-exist with (presumably younger) faults that are more optimally oriented for failure. We note that the 2019  $M_{\rm w}7.1$  mainshock nucleated on one of these more optimally oriented faults and proceeded to rupture a pre-existing less favourably oriented fault, suggestive of dynamic weakening<sup>28</sup>.

Our preferred model (Fig. 3b) is not sensitive to the time history of rotation of the principal stress axes. However, we note that the orientation of dikes of the Independence dike swarm (Fig. 4 and Supplementary Fig. 9) is consistent with the sense of rotation inferred from our analysis (Fig. 3b). Given that a direction normal to a dike plane marks the paleo-axis of the least compressive stress<sup>42</sup>, the angle between the axis of the present-day least compressive stress (orthogonal to the axis of  $\sigma_{\rm Hmax}$ , see Fig. 2) and the least compressive stress acting at the time of the dike intrusion is  $\alpha \approx 60-70^{\circ}$  (Fig. 4 and Supplementary Fig. 9). Dividing  $\alpha$  by the dike age of around 150 Myr (ref. 40) yields an apparent rotation rate of the principal stress axes on the order of 0.4-0.5° Myr<sup>-1</sup>, a factor of between two and five smaller than the average rotation rate of  $\sigma_{\rm Hmax}$ over the past 5-10 Myr (1-2° Myr<sup>-1</sup>, Fig. 3b). The former rate is an upper bound because some fraction of  $\alpha$  is likely due to axial shortening, rather than the absolute rotation of the principal stress axes. It follows that the clockwise rotation of the principal stress axes was occurring well before the initiation of the ECSZ, but substantially accelerated over the past 5-10 Myr.

A kinematic model of the origin of cross-faults proposed in this study links the present-day fault geometry to the deformation history and age of the ECSZ constrained by geodetic and geologic observations, respectively. It may also be applicable to other areas of high-angle strike-slip conjugate faulting<sup>2,43</sup>, as well as the observed clustering of the dip angles of normal earthquakes in the continental<sup>38</sup> and oceanic<sup>22</sup> lithosphere.

# Online content

Any methods, additional references, Nature Research reporting summaries, source data, extended data, supplementary information, acknowledgements, peer review information; details of author contributions and competing interests; and statements of data and code availability are available at https://doi.org/10.1038/s41561-021-00758-5.

Received: 14 July 2020; Accepted: 14 April 2021; Published online: 3 June 2021

#### References

- Anderson, E. M. The Dynamics of Faulting and Dike Formation with Application to Britain (Oliver and Boyd, 1951).
- 2. Scholz, C. H. *The Mechanics of Earthquakes and Faulting* 3rd edn (Cambridge Univ. Press, 2019).
- 3. Byerlee, J. Friction of rock. Pure Appl. Geophys. 116, 615–626 (1978).
- Sibson, R. H. Rupture nucleation on unfavorably oriented faults. Bull. Seism. Soc. Am. 80, 1580–1604 (1990).
- Lockner, D. A., Byerlee, J., Kuksenko, V., Ponomarev, A. & Sidorin, A. in Fault Mechanics and Transport Properties of Rocks (eds Evans, B. & Wong, T.) 3–31 (Academic, 1992).
- Walsh, J. & Watterson, J. Dips of normal faults in British Coal Measures and other sedimentary sequences. J. Geol. Soc. 145, 859–873 (1988).
- Collettini, C. & Sibson, R. H. Normal faults, normal friction? Geology 29, 927–930 (2001).
- Mount, V. & Suppe, J. State of stress near the San Andreas fault: implications for wrench tectonics. *Geology* 15, 1143–1146 (1987).
- Zoback, M. D. et al. New evidence on the state of stress of the San Andreas fault system. Science 238, 1105–1111 (1987).
- Wernicke, B. Low-angle normal faults and seismicity: a review. J. Geophys. Res. 100, 20159–20174 (1995).
- 11. Wang, K. & Fialko, Y. Observations and modeling of coseismic and postseismic deformation due to the 2015  $M_{\scriptscriptstyle w}$  7.8 Gorkha (Nepal) earthquake. J. Geophys. Res. 123, 761–779 (2018).

 Ron, H., Beroza, G. & Nur, A. Simple model explains complex faulting. Eos 82, 125–129 (2001).

- 13. Sibson, R. Reverse fault rupturing: competition between non-optimal and optimal fault orientations. *Geol. Soc. Spec. Publ.* **367**, 39–50 (2012).
- Wintsch, R., Christoffersen, R. & Kronenberg, A. Fluid-rock reaction weakening of fault zones. J. Geophys. Res. 100, 13021–13032 (1995).
- Faulkner, D. R., Mitchell, T. M., Healy, D. & Heap, M. J. Slip on 'weak' faults by the rotation of regional stress in the fracture damage zone. *Nature* 444, 922–925 (2007).
- Noda, H., Dunham, E. & Rice, J. R. Earthquake ruptures with thermal weakening and the operation of major faults at low overall stress levels. *J. Geophys. Res.* 114, B07302 (2009).
- 17. Di Toro, G. et al. Fault lubrication during earthquakes. *Nature* **471**, 494–498
- Han, R., Hirose, T. & Shimamoto, T. Strong velocity weakening and powder lubrication of simulated carbonate faults at seismic slip rates. J. Geophys. Res. 115, B03412 (2010).
- Brown, K. M. & Fialko, Y. 'Melt welt' mechanism of extreme weakening of gabbro at seismic slip rates. *Nature* 488, 638–641 (2012).
- Fialko, Y. in *Treatise on Geophysics* 2nd edn, Vol. 4 (ed. Schubert, G.) 73–91 (Elsevier, 2015).
- Chester, J. S., Chester, F. M. & Kronenberg, A. K. Fracture surface energy of the Punchbowl fault, San Andreas system. *Nature* 437, 133–136 (2005).
- Copley, A. The strength of earthquake-generating faults. J. Geol. Soc. 175, 1–12 (2018).
- Mitchell, E., Fialko, Y. & Brown, K. M. Velocity-weakening behavior of Westerly granite at temperature up to 600°C. J. Geophys. Res. 121, 6932–6946 (2016)
- Angelier, J. Tectonic analysis of fault slip data sets. J. Geophys. Res. 89, 5835–5848 (1984).
- Nicholson, C., Seeber, L., Williams, P. & Sykes, L. R. Seismic evidence for conjugate slip and block rotation within the San Andreas fault system, southern California. *Tectonics* 5, 629–648 (1986).
- 26. Ross, Z. E. et al. Hierarchical interlocked orthogonal faulting in the 2019 Ridgecrest earthquake sequence. *Science* **366**, 346–351 (2019).
- Chen, K. et al. Cascading and pulse-like ruptures during the 2019 Ridgecrest earthquakes in the Eastern California Shear Zone. *Nat. Commun.* 11, 22 (2020).
- Jin, Z. & Fialko, Y. Finite slip models of the 2019 Ridgecrest earthquake sequence constrained by space geodetic data and aftershock locations. *Bull. Seismol. Soc. Am.* 110, 1660–1679 (2020).
- Magen, Y., Ziv, A., Inbal, A., Baer, G. & Hollingsworth, J. Fault rerupture during the July 2019 Ridgecrest earthquake pair from joint slip inversion of InSAR, optical Imagery, and GPS. *Bull. Seismol. Soc. Am.* 110, 1627–1643 (2020).
- 30. Ponti, D. et al. Documentation of surface fault rupture and ground-deformation features produced by the 4 and 5 July 2019  $M_{\rm w}$  6.4 and  $M_{\rm w}$  7.1 Ridgecrest earthquake sequence. *Seismol. Res. Lett.* **91**, 2942–2959 (2020).
- Yang, W. & Hauksson, E. The tectonic crustal stress field and style of faulting along the Pacific North America Plate boundary in Southern California. Geophys. J. Int. 194, 100–117 (2013).
- Templeton, E. L. & Rice, J. R. Off-fault plasticity and earthquake rupture dynamics: 1. Dry materials or neglect of fluid pressure changes. *J. Geophys. Res.* 113, B09306 (2008).
- Takeuchi, C. & Fialko, Y. Dynamic models of interseismic deformation and stress transfer from plate motion to continental transform faults. J. Geophys. Res. 117, B05403 (2012).
- Montesi, L. Fabric development as the key for forming ductile shear zones and enabling plate tectonics. J. Struct. Geol. 50, 254–266 (2013).
- Takeuchi, C. & Fialko, Y. On the effects of thermally weakened ductile shear zones on postseismic deformation. J. Geophys. Res. 118, 6295–6310 (2013).
- Fialko, Y. & Simons, M. Deformation and seismicity in the Coso geothermal area, Inyo County, California: observations and modeling using satellite radar interferometry. J. Geophys. Res. 105, 21781–21793 (2000).
- 37. Nur, A., Ron, H. & Scotti, O. Fault mechanics and the kinematics of block rotations. *Geology* 14, 746–749 (1986).
- Thatcher, W. & Hill, D. P. Fault orientations in extensional and conjugate strike-slip environments and their implications. *Geology* 19, 1116–1120 (1991)
- Dokka, R. K. & Travis, C. J. Role of the Eastern California shear zone in accommodating Pacific-North American plate motion. *Geophys. Res. Lett.* 17, 1323–1327 (1990).
- Chen, J. H. & Moore, J. G. Late Jurassic Independence dike swarm in eastern California. Geology 7, 129–133 (1979).
- 41. Savage, J., Gan, W. & Svarc, J. Strain accumulation and rotation in the Eastern California Shear Zone. *J. Geophys. Res.* **106**, 21995–22007 (2001).
- Fialko, Y. A. & Rubin, A. M. Thermal and mechanical aspects of magma emplacement in giant dike swarms. J. Geophys. Res. 104, 23033–23049 (1999).

ARTICLES NATURE GEOSCIENCE

- Hudnut, K. W., Seeber, L. & Pacheco, J. Cross-fault triggering in the November 1987 Superstition Hills earthquake sequence, southern California. Geophys. Res. Lett. 16, 199–202 (1989).
- 44. Jennings, C. & Bryant, W. Fault Activity Map of California Geologic Data Map No. 6 (California Division of Mines and Geology, 2010).
- Fialko, Y. Probing the mechanical properties of seismically active crust with space geodesy: study of the coseismic deformation due to the 1992 M<sub>w</sub>7.3 Landers (southern California) earthquake. J. Geophys. Res. 109, B03307 (2004).
- Hauksson, E., Yang, W. & Shearer, P. M. Waveform relocated earthquake catalog for southern California (1981 to June 2011). *Bull. Seismol. Soc. Am.* 102, 2239–2244 (2012).

**Publisher's note** Springer Nature remains neutral with regard to jurisdictional claims in published maps and institutional affiliations.

© The Author(s), under exclusive licence to Springer Nature Limited 2021

NATURE GEOSCIENCE ARTICLES

### Methods

The horizontal coseismic surface displacements shown in Fig. 1b were computed by inverting synthetic aperture radar (or SAR) data that represent diverse projections of the surface displacement field<sup>47,48</sup>, including line-of-sight displacements (Sentinel-1A/B and ALOS-2 interferograms), range offsets (Sentinel-1A/B) and azimuth offsets (Cosmo-Skymed), from ascending and descending satellite tracks. The input data are from ref. 28 (see also the 'Data availability' section). To reduce speckle, the offset maps were filtered using a 1 km Gaussian filter. For each pixel we formed a system of linear equations by adding the respective unit look vectors as rows to the design matrix and the observed quantity to the data vector. The system was inverted to obtain the three orthogonal components of the displacement vector subject to two conditions: (1) more than two observations from different data sets are available for a given pixel and (2) a condition number of the design matrix is less than some threshold (150 in our calculations). The first condition ensures that the system is not under-determined; the second condition ensures that there is sufficient diversity in the look angles (that is, the solution is not highly unstable with respect to the data errors).

To analyse secular deformation in the Ridgecrest area, we used data from the continuously recording GNSS sites of PBO within approximately 200 km from the 2019 mainshock (Supplementary Fig. 3). We used solutions for daily positions provided by the UNAVCO community. The data were screened using the following criteria: (1) the site must have been in operation for the past 15 years (since 2004, to minimize transients from the 1992 Landers and 1999 Hector Mine earthquakes35) and (2) over the respective time period, the amount of missing data is less than 30%. After the initial quality checking of the data, we eliminated sites for which the displacement time series exhibited strong non-linear behaviour (for example, site HIVI). We also excluded site COSO, whose secular velocities are affected by production at the nearby geothermal plant<sup>36,49</sup>. Sites that were used in the analysis of secular deformation are shown as blue triangles in Supplementary Fig. 3. To compute secular velocities, we first cleaned up the UNAVCO time series by removing outliers and offsets (Supplementary Fig. 4). We then fitted a linear function to the cleaned time series for each component of the displacement vector. The slope of the best-fit line represents a respective component (that is, east (E) or north (N)) of the secular velocity vector. We verified the robustness of the derived velocity field by predicting the secular velocity at site TOWG, which is closest to the mainshock epicentre (see Supplementary Fig. 3) but was excluded from the analysis because it was installed only five years ago. The interpolated secular velocities show a good agreement with the observed time series at site TOWG (Supplementary Fig. 5), indicating that the derived velocity field is accurate and has a predictive power at spatial scales that are less than the distance between the continuous GNSS sites used in the analysis.

To compute the strain rate and rotation rate tensors from the secular velocities, we used Delaunay triangulation to identify the nearest GNSS sites (Supplementary Fig. 6). For each triplet of sites forming vertices of the Delaunay triangles, we subtracted the velocity of one site from the velocities of the remaining two sites. Assuming that the strain rate and the rotation rate are constant within a triangle, this gives rise to a system of four linear equations with four unknowns,  $\mathbf{v}_i = \dot{e}_{ij}\mathbf{x}_j + \omega_{ij}\mathbf{x}_j$ , where i and j are the components along the respective coordinate axis,  $\dot{e}_{ij}$  is the two-dimensional strain rate tensor,  $\omega_{ij}$  is the rotation rate tensor (anti-symmetric with zero diagonal components),  $\mathbf{x}_j$  is the baseline vector from the reference site and summation is implied over repeating indices. After obtaining the components of the strain rate tensor at each resolution cell, we computed the magnitude  $\dot{e}_{\mathrm{Hmax}}$  and orientation  $\phi$  of the principal shortening rate as follows:  $\dot{e}_{\mathrm{Hmax}} = 0.5 \left(\dot{e}_{\mathrm{EE}} + \dot{e}_{\mathrm{NN}} - \left[\left(\dot{e}_{\mathrm{EE}} + \dot{e}_{\mathrm{NN}}\right)^2 + \dot{e}_{\mathrm{EN}}^2\right]^{1/2}\right)$ ,  $\phi = 0.5 (\mathrm{arctan}[\dot{e}_{\mathrm{EN}}/(\dot{e}_{\mathrm{EE}} - \dot{e}_{\mathrm{NN}})] + \pi)$  (see Supplementary Fig. 6).

## Data availability

All data used in this study are open access. The first motion focal mechanism of the 2019  $M_{\rm w}$  7.1 mainshock is available at https://earthquake.usgs.gov/earthquakes/eventpage/ci38457511/focal-mechanism. The seismic moment of the 2019  $M_{\rm w}$  7.1 mainshock is available at https://earthquake.usgs.gov/earthquakes/eventpage/ci38457511/moment-tensor. The seismic moment of the 2019  $M_{\rm w}$  6.4 foreshock is available at https://earthquake.usgs.gov/earthquakes/eventpage/ci38443183/moment-tensor. The waveform-relocated earthquake catalog for southern California from ref.  $^{47}$  is available at https://scedc.caltech.edu/research-tools/alt-2011-dd-hauksson-yang-shearer.html. The GNSS position time series from the PBO is available at https://doi.org/10.7283/P2HT0Z. The coseismic displacement data and fault slip models from ref.  $^{28}$  are available at https://doi.org/10.5281/zenodo.4646321.

### Code availability

MATLAB codes used to generate results presented in this study are available at https://doi.org/10.5281/zenodo.4646292

#### References

- Fialko, Y., Simons, M. & Agnew, D. The complete (3-D) surface displacement field in the epicentral area of the 1999 M<sub>w</sub>7.1 Hector Mine earthquake, southern California, from space geodetic observations. *Geophys. Res. Lett.* 28, 3063–3066 (2001).
- Fialko, Y., Sandwell, D., Simons, M. & Rosen, P. Three-dimensional deformation caused by the Bam, Iran, earthquake and the origin of shallow slip deficit. *Nature* 435, 295–299 (2005).
- Tymofyeyeva, E. & Fialko, Y. Mitigation of atmospheric phase delays in InSAR data, with application to the eastern California shear zone. *J. Geophys. Res.* 120, 5952–5963 (2015).
- Wessel, P., Smith, W. H. F., Scharroo, R., Luis, J. & Wobbe, F. Generic Mapping Tools: improved version released. *Eos* 94, 409–410 (2013).

## **Acknowledgements**

We thank O. Zielke and M.-H. Huang for their comments. This study was supported by NSF (grants EAR-1841273 and EAR-1945760) and NASA (grant 80NSSC18K0466). Figures were produced using Generic Mapping Tools and MATLAB.

## **Author contributions**

Y.F. performed the data analysis and wrote the manuscript. Z.J. provided a finite fault model of the 2019 Ridgecrest earthquakes and contributed to the graphics design.

## **Competing interests**

The authors declare no competing interests.

#### Additional information

**Supplementary information** The online version contains supplementary material available at https://doi.org/10.1038/s41561-021-00758-5.

Correspondence and requests for materials should be addressed to Y.F.

**Peer review information** *Nature Geoscience* thanks Olaf Zielke and Mong-Han Huang for their contribution to the peer review of this work. Primary Handling Editor: Stefan Lachowycz.

Reprints and permissions information is available at www.nature.com/reprints.